ARTICLES
https://doi.org/10.1038/s41567-021-01194-3

nature physics

Domain-wall confinement and dynamics in a quantum simulator

W. L. Tan[1,3]✉, P. Becker[1,3]✉, F. Liu[1], G. Pagano[1,2], K. S. Collins[1], A. De[1], L. Feng[1], H. B. Kaplan[1], A. Kyprianidis[1], R. Lundgren[1], W. Morong[1], S. Whitsitt[1], A. V. Gorshkov[1] and C. Monroe[1]

Particles subject to confinement experience an attractive potential that increases without bound as they separate. A prominent example is colour confinement in particle physics, in which baryons and mesons are produced by quark confinement. Confinement can also occur in low-energy quantum many-body systems when elementary excitations are confined into bound quasiparticles. Here we report the observation of magnetic domain-wall confinement in interacting spin chains with a trapped-ion quantum simulator. By measuring how correlations spread, we show that confinement can suppress information propagation and thermalization in such many-body systems. We quantitatively determine the excitation energy of domain-wall bound states from the non-equilibrium quench dynamics. We also study the number of domain-wall excitations created for different quench parameters, in a regime that is difficult to model with classical computers. This work demonstrates the capability of quantum simulators for investigating high-energy physics phenomena, such as quark collision and string breaking.

Fundamental constituents of matter, such as quarks, cannot be observed in isolation, because they are permanently confined into bound states of mesons or baryons. Although the existence of confinement in particle physics is well established, quantitative understanding of the connection between theoretical prediction and experimental observation remains an active area of research[1,2]. Similar phenomena can occur in low-energy quantum many-body systems, which can provide insight into confinement from a microscopic perspective. The static and equilibrium properties of such confined systems have been well characterized in previous theoretical[3–5] as well as experimental works[6,7]. However, recent theoretical studies have demonstrated that confinement can also have dramatic consequences for the out-of-equilibrium dynamics of quantum many-body systems, such as suppression of information spreading and slow thermalization[8–15].

Quantum simulators allow the study of out-of-equilibrium physics of quantum many-body systems in a well-controlled environment[16,17]. An emerging application of these simulators is the study of problems motivated by high-energy physics and gauge theories[18–24]. Here, we use trapped-ion quantum simulators[25–28] to directly observe real-time domain-wall confinement dynamics in a spin chain following a quantum quench, or sudden change in the Hamiltonian (Fig. 1). We show that confinement can suppress the spreading of correlations even in the absence of disorder, and that quench dynamics can be used to characterize the excitation energies of confined bound states. We also measure the number of domain walls generated by a global quench, in and out of the confinement regime. Finally, we demonstrate that the number of domain walls can be an effective probe of the transition between two distinct dynamical regimes[29,30].

Confinement in many-body systems occurs in one of the classic models of statistical mechanics: the Ising spin chain with both transverse and longitudinal magnetic fields. A non-zero longitudinal field confines pairs of originally freely propagating domain-wall quasiparticles into meson-like bound states in a system of short-range interactions[8,10,12]. However, recent theoretical efforts[9,11] have demonstrated that long-range Ising interactions, instead of an additional longitudinal field, can naturally induce a confining potential between pairs of domain walls (Fig. 1a). As a consequence of confinement, the low-energy spectrum of such an Ising system can feature meson-like bound domain-wall quasiparticles (Fig. 1a)[8,11], similar to confinement in quantum chromodynamics (QCD), where quarks and antiquarks are confined into hadrons owing to strong interactions. In both cases, confining potentials increase asymptotically with particle separation, although with differing power-law forms. Similarly to QCD, domain-wall confinement in the long-range Ising model studied here includes a discrete spectrum of bound states, string breaking[14] (or particle/antiparticle creation) and a confinement–deconfinement crossover as a function of energy density[2,31]. Although this model does not include other aspects of QCD, such as gauge fields or chiral symmetry breaking, the similarity of the confinement mechanisms allows us to draw broadly applicable conclusions about this effect.

We used a trapped-ion quantum simulator to investigate confinement in a many-body spin system governed by the Hamiltonian ($\hbar = 1$)

$$H = -\sum_{i<j}^{L} J_{i,j}\sigma_i^x\sigma_j^x - B\sum_i^L \sigma_i^z. \quad (1)$$

Here, σ_i^γ ($\gamma = x, y, z$) is the Pauli operator acting on the ith spin, $J_{i,j} \approx J_0/|i-j|^\alpha$ is the power-law decaying Ising coupling between spins i and j with tunable exponent α, $J_0 > 0$, B is the effective transverse field and L is the number of spins[32,33] (Methods). We encoded each spin in the ground-state hyperfine levels $|\uparrow\rangle_z \equiv |F = 1, m_F = 0\rangle$ and $|\downarrow\rangle_z \equiv |F = 0, m_F = 0\rangle$ of the $^2S_{1/2}$ manifold of a $^{171}Yb^+$ ion. The Ising couplings are produced via spin-dependent optical dipole forces, with α ranging from 0.8 to 1.1 and $J_0/2\pi$ ranging from 0.23 kHz to 0.66 kHz (Methods).

To study the real-time dynamics of the spin chain, we used a quantum quench to bring the system out of equilibrium (Fig. 1b). We first initialized the spins in a product state, polarized either along

[1]Joint Quantum Institute and Joint Center for Quantum Information and Computer Science, University of Maryland and NIST, College Park, MD, USA. [2]Present address: Department of Physics and Astronomy, Rice University, Houston, TX, USA. [3]These authors contributed equally: W. L. Tan, P. Becker. ✉e-mail: wltan93@terpmail.umd.edu; pbecker1@terpmail.umd.edu

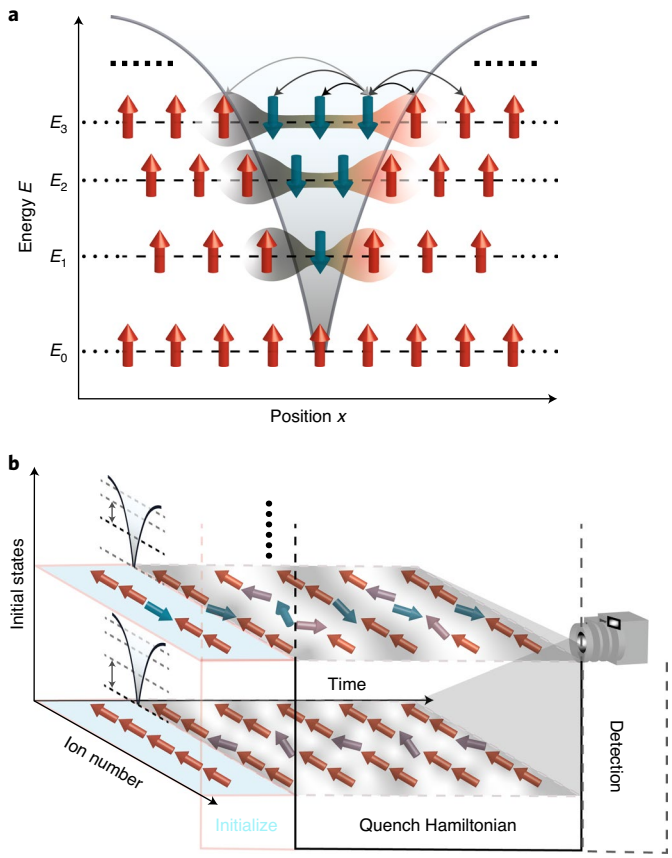

Fig. 1 | Effective confining potential and experiment sequence. a, Magnetic domain walls in Ising spin chains can experience an effective confining potential that increases with distance analogously to the strong nuclear force. This potential results in meson-like domain-wall bound states (labelled E_1 to E_3, with initial state E_0) that can dramatically influence the dynamics of the system[11,12]. The grey arrows indicate long-range interactions between spins, where the opacity reflects interaction strengths that weaken with distance (interaction arrows are not shown for all spins). The shaded regions indicate interacting domain-wall quasiparticles. The dotted lines represent the extension of this model to larger systems. **b**, This experiment begins by initializing a chain of trapped-ion spins in a product state. We introduce pairs of domain walls by flipping the initial states of chosen spins. The spins evolve according to the quenched Hamiltonian through time, after which we measure various observables, such as the magnetization of each individual spin along a desired axis. The grey double-ended arrows represent energy differences between two adjacent energy levels corresponding to a particular initial state.

the x or z directions of the Bloch sphere. Using a tightly focused individual addressing laser[34], we prepared domain walls in various initial state configurations (Fig. 2c,f,i). After preparing the desired initial state, we performed a sudden quench of the Hamiltonian (1). For $B/J_0 \approx 0.75$, the quench optimally drives the system out of equilibrium while remaining in the confinement regime. Following the evolution of the system through time (t), we used spin-dependent fluorescence to measure the state of each spin. From this data, we calculated the time evolution of magnetizations, $\langle \sigma_i^x(t) \rangle$ or $\langle \sigma_i^z(t) \rangle$, and connected correlations

$$C_{i,j}^x(t) = \left\langle \sigma_i^x(t)\sigma_j^x(t) \right\rangle - \langle \sigma_i^x(t) \rangle \left\langle \sigma_j^x(t) \right\rangle. \quad (2)$$

No post-processing or state preparation and measurement correction have been applied to any of the data reported below.

To understand the effect of confinement on information spreading, we measured the absolute value of connected correlations along x, the Ising direction (Fig. 2). When the initial state contains a small number of domain walls, correlations spread with a considerably smaller velocity than the velocity in a corresponding nearest-neighbour interacting system[8] ($v_0 = 4B$, Fig. 2). Correlation functions typically exhibit a light-cone behaviour following a quantum quench[35–37], whereas we observed strongly suppressed spreading and localized correlations throughout the evolution[10,15]. This indicates that confinement, induced by long-range interactions, localizes pairs of domain walls at their initial conditions (Supplementary Information).

In stark contrast, we found that correlations exhibit faster-than-linear spreading, despite quenching under the same Hamiltonian, in the case of the initial state polarized in the transverse direction z (Fig. 2g–i). In this case, the initial state was a linear superposition of all possible spin configurations in the x direction, and thus contained a large number of domain walls. Unlike the previous initial states, this initial state had an energy density relatively far from the bottom of the many-body spectrum. The long-range interactions among these domain walls led to fast relaxation and quantum information spreading. These results imply that this confinement effect has a substantial impact only on the low-energy excitations of the system, which is consistent with recent theoretical studies[8–12].

To observe the effect of confinement on the thermalization of local observables, we measured the relaxation of magnetizations for the above initial states[38] (third row of Fig. 2). We see that, for the low-energy states, local magnetizations retain long memories of their initial configuration and exhibit slow relaxation (Fig. 2c,f). Conversely, for the high-energy initial state, local magnetizations quickly relax to their thermal expectation values (Fig. 2i and Supplementary Information). This is consistent with the observation that correlations quickly distribute across the entire system (Fig. 2h). We emphasize that the observed slow thermalization is a consequence of confinement, distinct from many-body localization with quenched disorder[39–41].

To quantitatively probe excitation energies of bound domain-wall states, we prepared initial states polarized along the x direction and varied the number of spins separating the two initial domain walls (insets of Fig. 3a–c). Then, we quenched the system under Hamiltonian (1) and measured the time evolution of local magnetizations along the transverse direction $\langle \sigma_i^z(t) \rangle$. In the confinement regime, the prepared initial states predominantly overlapped with low-energy eigenstates of the confinement Hamiltonian[11]. All local observables should exhibit oscillations with frequencies proportional to the energy gap between these bound states before thermalizing[8,11]. Here, we chose a single-body spin observable, $\langle \sigma_i^z(t) \rangle$, at the centre of the chain (for zero initial domain walls) or at the outer boundaries of the initial domain (for two initial domain walls). We made this particular choice to minimize edge effects from the finite spin chain and maximize the matrix elements of this observable between the prepared state i and the adjacent higher-energy bound state $i+1$ (Fig. 1a), allowing us to extract the energy gap between these two states (Methods).

Following this prescription, we extracted oscillation frequencies using single-frequency sinusoidal fits of $\langle \sigma_i^z(t) \rangle$ to obtain the energy gap between each initialized state and the neighbouring excited state (Fig. 3a–c). We compared these extracted energies to values predicted by numerical simulations (Methods). We found excellent agreement between the measured energies and the energies predicted numerically (Fig. 3d). Using these experimentally measured energy gaps, we could systematically construct the low-energy excitation spectrum of the many-body system for quasimomentum $k \approx 0$ (Fig. 3e). In general, quasiparticles with arbitrary quasimomenta can be excited by a quantum quench. However, as the confining

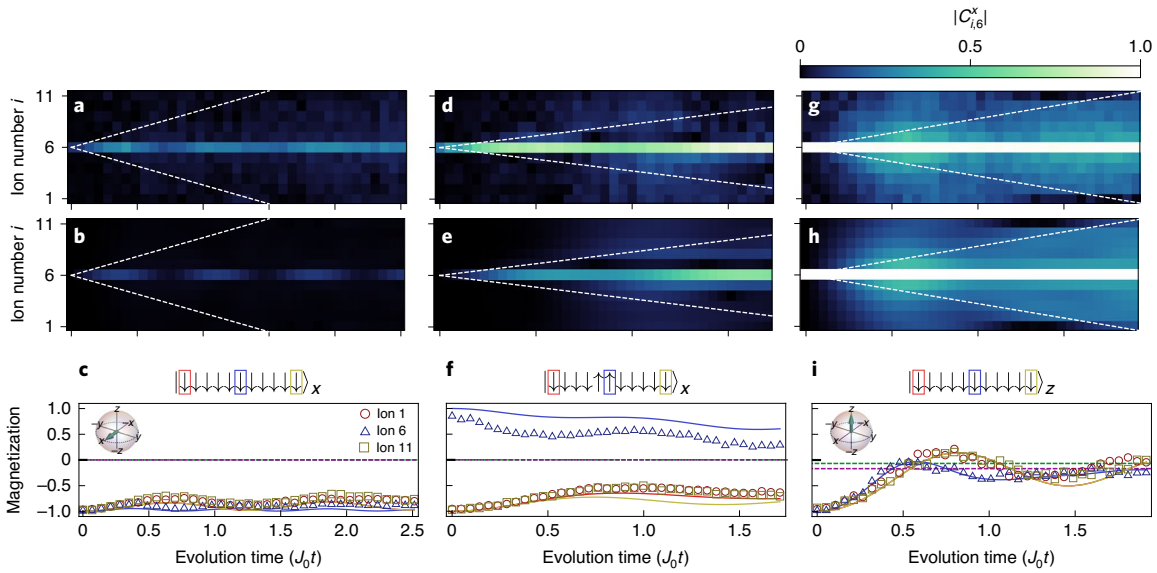

Fig. 2 | Confinement dynamics at $B/J_0 \approx 0.75$, $L = 11$. **a**,**d**,**g**, $|C^x_{i,6}(t)|$ averaged over 2,000 experiments. **b**,**e**,**h**, $|C^x_{i,6}(t)|$ calculated by solving the Schrödinger equation. Dashed white lines show correlation propagation bounds (light cones) in the limit $\alpha \to \infty$ (nearest-neighbour interactions). **c**,**f**,**i**, Measured $\langle \sigma_i^{x,z}(t) \rangle$ averaged over 2,000 experiments for **c** and **f** and 400 experiments for **i**. Symbols represent magnetization data and solid coloured curves represent theoretical magnetizations calculated by solving the Schrödinger equation. All magnetization error bars (±1 s.d.) are smaller than the symbols and are not shown. Purple (green) dashed lines represent thermal expectation values calculated from a canonical (microcanonical) ensemble averaged over the three displayed spins (Supplementary Information). The spin diagrams above **c**, **f** and **i** depict the initial states prepared along the axes of the Bloch sphere shown by the inset diagrams. **c** and **f** are prepared along x (sharing the same inset) and **i** is prepared along z. The boxed spins represent selected magnetization dynamics. **a**–**c**, A low-energy initial state containing zero domain walls. Individual magnetizations are $\langle \sigma_i^x(t) \rangle$. **d**–**f**, A low-energy initial state containing two domain walls, with a centre domain of two spins. Individual magnetizations are $\langle \sigma_i^x(t) \rangle$. We attribute the discrepancy between the experimental magnetization data and numerical predictions to imperfect state initialization. **g**–**i**, A high-energy initial state containing many domain walls. Individual magnetizations are $\langle \sigma_i^z(t) \rangle$. **a**–**c**, **d**–**f** and **g**–**i** share their respective x axes.

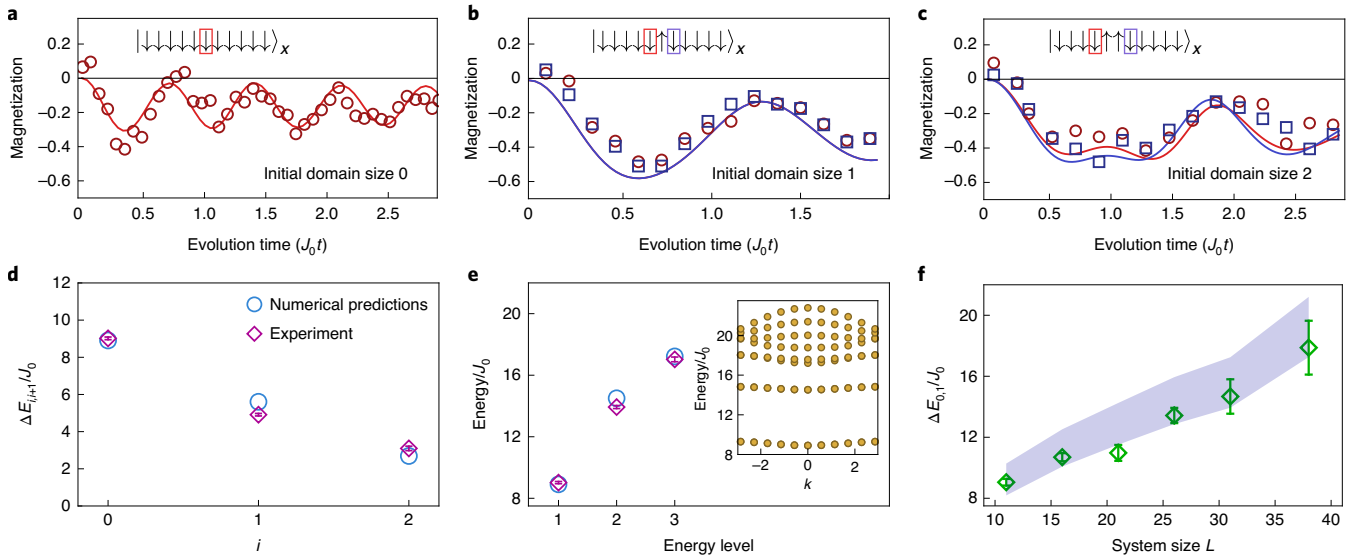

Fig. 3 | Low-energy excited states. **a**–**c**, Magnetizations of the boxed spins on the edges of the centre domain at $B/J_0 \approx 0.75$. These magnetization oscillation frequencies correspond to the normalized energy gap $\Delta E_{i,i+1}/J_0$. Solid coloured lines represent theoretical calculations of dynamics by solving the Schrödinger equation. **a**, Zero initial domain size: $\Delta E_{0,1}/J_0$ is given by the frequency of the sixth spin. **b**, Initial domain size of one: $\Delta E_{1,2}/J_0$ is given by the frequency of the fifth and seventh spins. **c**, Initial domain size of two: $\Delta E_{2,3}/J_0$ is given by the frequency of the fourth and seventh spins. **d**, $\Delta E_{i,i+1}/J_0$ for $i \leq 2$ measured with three different initial domain-size spin configurations at $B/J_0 \approx 0.75$. The first three energy gaps ($i \leq 2$) were extracted from the magnetization oscillation frequencies shown in **a**–**c**. **e**, Bound-state energy levels (labelled Energy/J_0) at $k \approx 0$ constructed using experimental data shown in **d**, where E_0/J_0 is set to zero. Theoretical bound-state energy bands with different k within the two-domain-wall model[11] are shown in the inset (Methods). **f**, Scaling of $\Delta E_{0,1}/J_0$ with system size L at $B/J_0 \approx 1$. The blue shaded region shows the two-domain-wall model[11] (Methods) numerical prediction of $\Delta E_{0,1}/J_0$, with a confidence band considering ±10% fluctuations in J_0. The error bars represent ±1 s.d. and are smaller than the symbols in **a**–**c**.

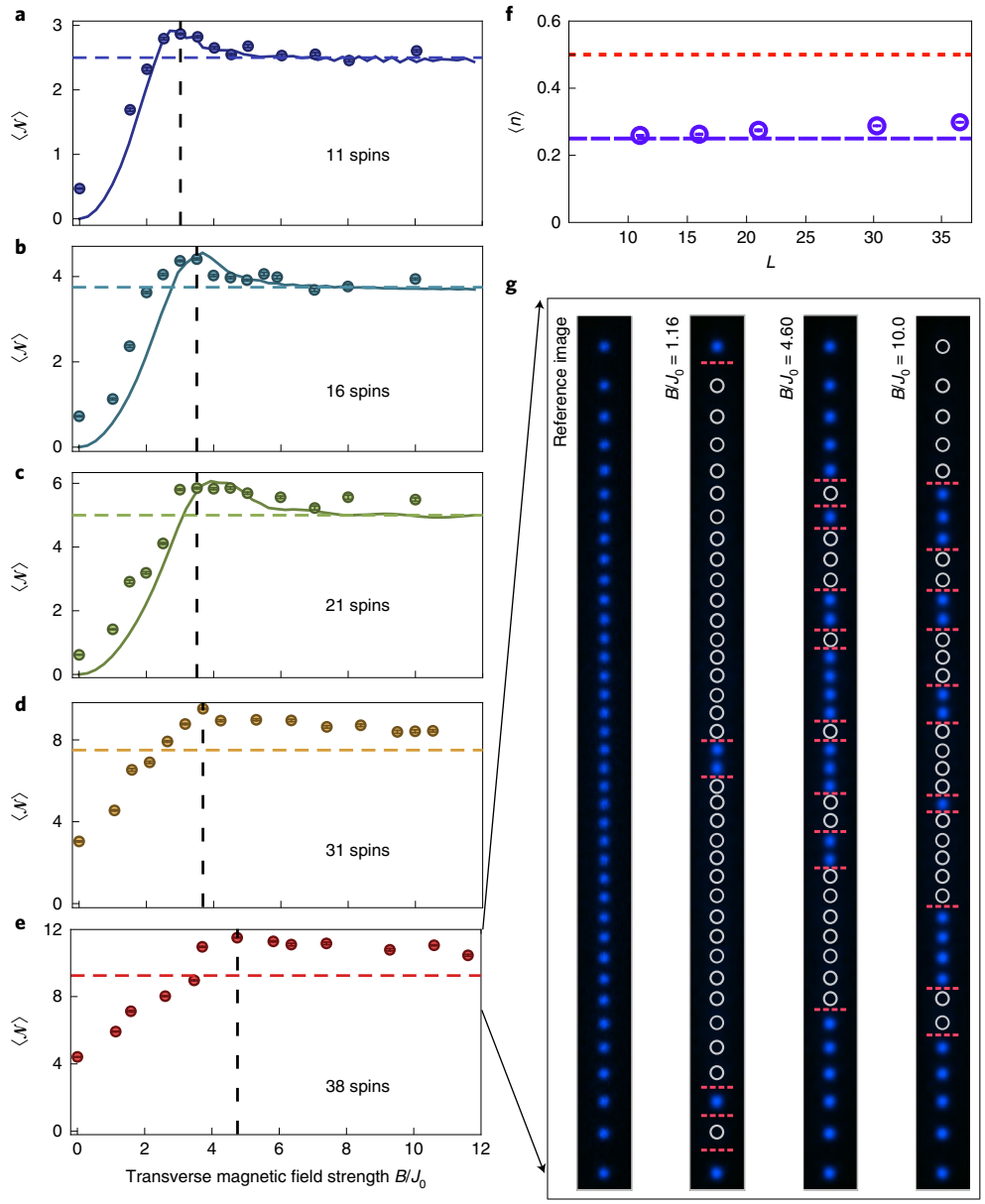

Fig. 4 | Number of domain walls in two dynamical regimes. a–e, Two dynamical regimes with increasing transverse B field strength in systems of 11 (**a**), 16 (**b**), 21 (**c**), 31 (**d**) and 38 (**e**) spins. Dots indicate experimental data. Horizontal lines show theoretical predictions of $\langle \mathcal{N} \rangle = 0.25(L-1)$ at $B \gg J_0$. Solid curves represent numerical results predicted by solving the Schrödinger equation. Vertical dashed lines indicate the experimental maxima of $\langle \mathcal{N} \rangle$. Theoretical lines for system sizes $L = 31$ (**d**) and $L = 38$ (**e**) are absent because we cannot compute the predicted evolution numerically for the experimental parameters. **f**, Theoretical prediction of domain-wall density at $B \gg J_0$, $\langle n \rangle_{B \gg J_0}$ (dashed blue line). The blue dots indicate experimental data for the domain-wall density at $B \approx 10 J_0$, $\langle n \rangle_{B \approx 10 J_0}$. The dashed red line at $\langle n \rangle_T = 0.5$ shows the density of domain walls using the canonical ensemble at infinite temperature. All of the experimental data are integrated within the time interval $J_0 t_1 \approx 0.34$ and $J_0 t_2 \approx 0.73$. **g**, Reconstructed images based on the binary detection of spin states. The leftmost image is a reference image of a 38 ion chain in a bright state ($|\uparrow\rangle_x$). At the beginning of the experiment, the spins are initialized in the dark state ($|\downarrow\rangle_x$). The three right images show experimental data for a combination of bright and dark states (blue and white circles, respectively) for three different B/J_0 values within the integrated time frame. The occurrences of domain walls are highlighted with orange horizontal dashed lines. Error bars show ±1 s.d. for >150 experiments, all are smaller than the symbols.

potential is steep, excited quasiparticles remained localized and their quasimomenta were close to zero. Furthermore, leveraging the scalability of trapped-ion systems, we performed this experiment with up to 38 spins. To numerically investigate these large system sizes, we used a phenomenological two-domain-wall model[11] (Methods). With this model, by restricting the full Hilbert space to a subspace of states containing only zero or two domain walls, we calculated the bound quasiparticle spectrum of Hamiltonian (1) for system sizes that would be challenging to exactly simulate with classical resources (Fig. 3f). We found reasonable agreement in the first excitation energy gap, $\Delta E_{0,1}$, between the experimental data and numerical predictions for all system sizes (Fig. 3f). We attributed the systematic discrepancy in larger systems to variations in J_0 during the time evolution (Methods). These results, taken together, suggest that quench dynamics are dominated by the confinement effect between two-domain-wall quasiparticles.

We next went beyond the confinement regime to study the number of domain walls generated by the quantum quench for a wide

range of transverse B field strengths. Although we still prepared an initial state polarized along $|\downarrow\rangle_x$, for large B the strong quench can excite a large number of domain walls that are no longer bounded. We thus expected that the out-of-equilibrium dynamics would no longer be captured by the confinement picture for these parameters. To explore this regime, we measured the cumulative time average of the total number of domain walls

$$\langle \mathcal{N} \rangle = \frac{1}{t_2 - t_1} \int_{t_1}^{t_2} \sum_{i=1}^{L-1} \frac{\langle 1 - \sigma_i^x(t)\sigma_{i+1}^x(t) \rangle}{2}, \qquad (3)$$

where t_1 and t_2 enclose a window where $\langle \mathcal{N} \rangle$ converges to a stable value (Methods and Extended Data Fig.1). The expectation value was normalized by 1/2 to correctly count the number of domain walls between neighbouring spins[42]. We measured $\langle \mathcal{N} \rangle$ as a function of B for different system sizes (Fig. 4a–e). We observed that, for small B fields, Ising interactions dominated the dynamics and the global quench could only excite a small number of domain walls. However, for a large enough transverse field, the number of generated domain walls saturated to a value that scaled nearly linearly with system size (Fig. 4f). Here, we observed a transition between these two dynamical regimes at intermediate values of B for different system sizes. This behaviour is analogous to the confinement–deconfinement crossover conjectured in QCD, in which increasing energy density (controlled by B in this experiment) causes hadronic matter to form a quark–gluon plasma or other exotic phase[2]. In both models, beyond a critical energy density, weaker interactions allow particles to freely move with a negligible energy penalty.

To illustrate the population of domain walls in different regimes, we show typical single-shot images of the quenched state of 38 ions for different transverse B fields in Fig. 4g. We saw that a small (large) number of domain walls was generated by the quench with small (large) B field. Although we were unable to compute the dynamics for system size $L = 31$ and beyond with general-purpose computers, we can intuitively understand the distinguishing behaviours. When we increased B to values much larger than J_0, all spins underwent Larmor precession around the z axis of the Bloch sphere, which allows us to predict that $\langle \mathcal{N} \rangle$ saturates to $0.25(L-1)$ when $B \to \infty$ (ref. [43]) (Methods). We note that, for $B \gg J_0$, the experiment operated in the prethermal region in which a transient Hamiltonian is approximately conserved for an exponentially long time[44–47]. Therefore, we expected the number of domain walls to approach the thermal value $\langle n \rangle_T = 0.5$ only after an exponentially long time, beyond the reach of this experiment. The experimental results agree with the numerical prediction for system sizes within the reach of numerical simulations. We attribute the discrepancies at large system sizes to bit-flip events due to detection errors and off-resonant coupling to motional degrees of freedom (Methods and Extended Data Fig. 2), and to finite effective magnetic fields B compared with the total interaction energy[48], which increases with system size due to its long-range character.

In summary, we have presented a real-time observation of domain-wall confinement caused by long-range interactions in trapped-ion spin systems. By measuring oscillating magnetizations, we were able to construct the spectrum of low-energy domain-wall bound states. Furthermore, we observed a transition between distinct dynamical behaviours using the number of domain walls generated by the global quench. This work demonstrates that confinement, naturally induced by long-range interactions, may provide a novel mechanism for protecting quantum information without engineering disorder. Such a feature may be applied in future studies to use long-range interactions to stabilize non-equilibrium phases of matter. This work establishes the utility of trapped-ion quantum simulators for precisely studying real-time dynamics of many-body systems, potentially extending to exotic phenomena such as quark collision and string breaking[14].

Note added in proof: While finalizing this manuscript, we became aware of a complementary work on quasiparticle confinement with nearest-neighbour interactions[49].

Online content

Any methods, additional references, Nature Research reporting summaries, source data, extended data, supplementary information, acknowledgements, peer review information; details of author contributions and competing interests; and statements of data and code availability are available at https://doi.org/10.1038/s41567-021-01194-3.

Received: 4 November 2020; Accepted: 7 February 2021;
Published online: 18 March 2021

References

1. Greensite, J. *An Introduction to the Confinement Problem* 1–2 (Springer, 2011).
2. Brambilla, N. et al. QCD and strongly coupled gauge theories: challenges and perspectives. *Eur. Phys. J. C* **74**, 2981 (2014).
3. McCoy, B. M. & Wu, T. T. Two-dimensional Ising field theory in a magnetic field: breakup of the cut in the two-point function. *Phys. Rev. D* **18**, 1259–1267 (1978).
4. Delfino, G. & Mussardo, G. The spin-spin correlation function in the two-dimensional Ising model in a magnetic field at $T = T_C$. *Nucl. Phys. B* **455**, 724–758 (1995).
5. Fonseca, P. & Zamolodchikov, A. Ising spectroscopy I: mesons at $T < T_C$. Preprint at https://arxiv.org/abs/hep-th/0612304 (2006).
6. Lake, B. et al. Confinement of fractional quantum number particles in a condensed-matter system. *Nat. Phys.* **6**, 50–55 (2010).
7. Coldea, R. et al. Quantum criticality in an Ising chain: experimental evidence for emergent E_8 symmetry. *Science* **327**, 177–180 (2010).
8. Kormos, M., Collura, M., Takács, G. & Calabrese, P. Real-time confinement following a quantum quench to a non-integrable model. *Nat. Phys.* **13**, 246–249 (2017).
9. Lerose, A., Žunkovič, B., Silva, A. & Gambassi, A. Quasilocal excitations induced by long-range interactions in translationally invariant quantum spin chains. *Phys. Rev. B* **99**, 121112 (2019).
10. James, A. J. A., Konik, R. M. & Robinson, N. J. Nonthermal states arising from confinement in one and two dimensions. *Phy. Rev. Lett.* **122**, 130603 (2019).
11. Liu, F. et al. Confined quasiparticle dynamics in long-range interacting quantum spin chains. *Phys. Rev. Lett.* **122**, 150601 (2019).
12. Mazza, P. P., Perfetto, G., Lerose, A., Collura, M. & Gambassi, A. Suppression of transport in nondisordered quantum spin chains due to confined excitations. *Phys. Rev. B* **99**, 180302 (2019).
13. Lerose, A. et al. Quasilocalized dynamics from confinement of quantum excitations. *Phys. Rev. B* **102**, 041118 (2020).
14. Verdel, R., Liu, F., Whitsitt, S., Gorshkov, A. V. & Heyl, M. Real-time dynamics of string breaking in quantum spin chains. *Phys. Rev. B* **102**, 014308 (2020).
15. Santos, L. F., Borgonovi, F. & Celardo, G. L. Cooperative shielding in many-body systems with long-range interaction. *Phys. Rev. Lett.* **116**, 250402 (2016).
16. Feynman, R. P. Simulating physics with computers. *Int. J. Theor. Phys.* **21**, 467–488 (1982).
17. Georgescu, I. M., Ashhab, S. & Nori, F. Quantum simulation. *Rev. Mod. Phys.* **86**, 153–185 (2014).
18. Görg, F. et al. Realization of density-dependent Peierls phases to engineer quantized gauge fields coupled to ultracold matter. *Nat. Phys.* **15**, 1161–1167 (2019).
19. Schweizer, C. et al. Floquet approach to $\mathbb{Z}_2$ lattice gauge theories with ultracold atoms in optical lattices. *Nat. Phys.* **15**, 1168–1173 (2019).
20. Mil, A. et al. A scalable realization of local U(1) gauge invariance in cold atomic mixtures. *Science* **367**, 1128–1130 (2020).
21. Muschik, C. et al. U(1) Wilson lattice gauge theories in digital quantum simulators. *New J. Phys.* **19**, 103020 (2017).
22. Brenes, M., Dalmonte, M., Heyl, M. & Scardicchio, A. Many-body localization dynamics from gauge invariance. *Phys. Rev. Lett.* **120**, 030601 (2018).
23. Bañuls, M. C. et al. Simulating lattice gauge theories within quantum technologies. *Eur. Phys. J. D* **74**, 165 (2020).
24. Borla, U., Verresen, R., Grusdt, F. & Moroz, S. Confined phases of one-dimensional spinless fermions coupled to $\mathbb{Z}_2$ gauge theory. *Phys. Rev. Lett.* **124**, 120503 (2020).
25. Porras, D. & Cirac, J. I. Effective spin systems with trapped ions. *Phys. Rev. Lett.* **92**, 207901 (2004).
26. Bohnet, J. G. et al. Quantum spin dynamics and entanglement generation with hundreds of trapped ions. *Science* **352**, 1297–1301 (2016).
27. Jurcevic, P. et al. Direct observation of dynamical quantum phase transitions in an interacting many-body system. *Phys. Rev. Lett.* **119**, 080501 (2017).

28. Zhang, J. et al. Observation of a many-body dynamical phase transition with a 53-qubit quantum simulator. *Nature* **551**, 601–604 (2017).
29. Halimeh, J. C. & Zauner-Stauber, V. Dynamical phase diagram of spin chains with long-range interactions. *Phys. Rev. B* **96**, 134427 (2017).
30. Žunkovič, B., Heyl, M., Knap, M. & Silva, A. Dynamical quantum phase transitions in spin chains with long-range interactions: merging different concepts of nonequilibrium criticality. *Phys. Rev. Lett.* **120**, 130601 (2018).
31. Magnifico, G. et al. Real time dynamics and confinement in the $\mathbb{Z}_n$ Schwinger–Weyl lattice model for 1+1 QED. *Quantum* **4**, 281 (2020).
32. Kim, K. et al. Entanglement and tunable spin-spin couplings between trapped ions using multiple transverse modes. *Phys. Rev. Lett.* **103**, 120502 (2009).
33. Pagano, G. et al. Cryogenic trapped-ion system for large scale quantum simulation. *Quantum Sci. Technol.* **4**, 014004 (2018).
34. Lee, A. C. et al. Engineering large Stark shifts for control of individual clock state qubits. *Phys. Rev. A* **94**, 042308 (2016).
35. Calabrese, P. & Cardy, J. Time dependence of correlation functions following a quantum quench. *Phys. Rev. Lett.* **96**, 136801 (2006).
36. Cheneau, M. et al. Light-cone-like spreading of correlations in a quantum many-body system. *Nature* **481**, 484–487 (2012).
37. Eisert, J., Friesdorf, M. & Gogolin, C. Quantum many-body systems out of equilibrium. *Nat. Phys.* **11**, 124–130 (2015).
38. Bañuls, M. C., Cirac, J. I. & Hastings, M. B. Strong and weak thermalization of infinite nonintegrable quantum systems. *Phys. Rev. Lett.* **106**, 050405 (2011).
39. Schreiber, M. et al. Observation of many-body localization of interacting fermions in a quasirandom optical lattice. *Science* **349**, 842–845 (2015).
40. Nandkishore, R. & Huse, D. A. Many-body localization and thermalization in quantum statistical mechanics. *Annu. Rev. Condens. Matter Phys.* **6**, 15–38 (2015).
41. Hess, P. W. et al. Non-thermalization in trapped atomic ion spin chains. *Phil. Trans. R. Soc. A* **375**, 20170107 (2017).
42. del Campo, A. & Zurek, W. H. Universality of phase transition dynamics: topological defects from symmetry breaking. *Int. J. Mod. Phys. A* **29**, 1430018 (2014).
43. Calabrese, P., Essler, F.H.L. & Fagotti, M. Quantum quenches in the transverse field Ising chain: II. Stationary state properties. *J. Stat. Mech.* **2012**, P07022 (2012).
44. Abanin, D., Roeck, W. D., Ho, W. W. & Huveneers, F. A rigorous theory of many-body prethermalization for periodically driven and closed quantum systems. *Commun. Math. Phys.* **354**, 809–827 (2017).
45. Halimeh, J. C. et al. Prethermalization and persistent order in the absence of a thermal phase transition. *Phys. Rev. B* **95**, 024302 (2017).
46. Tran, M. C. et al. Locality and heating in periodically driven, power-law interacting systems. *Phys. Rev. A* **100**, 052103 (2019).
47. Machado, F., Else, D. V., Kahanamoku-Meyer, G. D., Nayak, C. & Yao, N. Y. Long-range prethermal phases of nonequilibrium matter. *Phys. Rev. X* **10**, 011043 (2020).
48. Essler, F. H. L., Kehrein, S., Manmana, S. R. & Robinson, N. J. Quench dynamics in a model with tuneable integrability breaking. *Phys. Rev. B* **89**, 165104 (2014).
49. Vovrosh, J. & Knolle, J. Confinement dynamics on a digital quantum computer. Preprint at https://arxiv.org/abs/2001.03044 (2020).

Methods

Trapped-ion quantum simulators. In this work, we used two quantum simulators that we refer to as System 1[32] and System 2[33]. System 1 is a room temperature trapped-ion apparatus. It employs a three-layer linear Paul trap with transverse centre-of-mass (COM) motional mode frequency $\nu_{\mathrm{COM}} = 4.7$ MHz and axial COM frequency $\nu_z \approx 0.5$ MHz (ref. [32]). The main limitation of this apparatus is the rate of collisions with the residual background gas in ultra-high vacuum, limiting the practical size of the chain. During such collision events, the ion crystal melts and ions are ejected from the trap due to radiofrequency heating. However, this apparatus has individual addressing capabilities, allowing for initialization of arbitrary spin flips, which is crucial in this work. Therefore, we used it to investigate low-energy domain-wall bound states in smaller system sizes.

System 2 is a linear blade Paul trap in a cryogenic environment with only global qubit control[33]. The trap is held at ~8 K in a closed cycle cryostat, where the background pressure is below 1.33×10^{-10} Pa owing to differential cryopumping. This allows for longer storage lifetimes of large ion chains compared with System 1. For this reason, System 2 can support larger chains to measure the lowest-bound-state energy and investigate the two distinct dynamical regimes by increasing the transverse B field. To take the anharmonicity of the trap into account, we measured all the transverse motional modes of the ion chain. The transverse motional frequencies were set to $\nu^x_{\mathrm{COM}} = 4.4$ MHz and $\nu^y_{\mathrm{COM}} = 4.3$ MHz, the x tilt frequency ν^x_{tilt} ranged from 4.37 MHz to 4.38 MHz and the y tilt frequency ν^y_{tilt} ranged from 4.24 MHz to 4.25 MHz depending on the number of trapped ions.

Initial state preparation. In both systems, every experiment began by Doppler cooling a chain of trapped $^{171}\mathrm{Yb}^+$ ions using 369.5 nm light red-detuned from the $^2S_{1/2}$ to $^2P_{1/2}$ transition. The ions were initialized to the $|\downarrow\rangle_z$ qubit state, defined as the $^2S_{1/2}|F = 0, m_F = 0\rangle$ hyperfine level, by an incoherent optical pumping process. Optical pumping lasted approximately 20 µs and initialized all ions to $|\downarrow\rangle_z$ with at least 99% fidelity. Next, the ions were cooled to their motional ground state ($\lesssim$0.1 average motional quanta for the COM mode) with Raman sideband cooling.

Once the spins were cooled and initialized, we could prepare them in product states along any axis of the Bloch sphere by applying global rotation pulses. System 1 has the ability to manipulate spins with an individual addressing beam focused to a waist of 500 nm, 3–4 times smaller than the typical inter-ion spacing in System 1. This beam applied a fourth-order a.c. Stark shift to the qubit splitting[34], causing an effective σ_i^z rotation on a single spin i. This rotation could be mapped to a rotation about any axis with global $\pi/2$-pulses, which allowed the preparation of product states with arbitrary spin flips.

State detection. Following the experiment, we measured each spin's magnetization using spin-dependent fluorescence imaged onto an Andor iXon Ultra 897 EMCCD camera. A 369.5 nm laser resonant with the $^2S_{1/2}|F = 1\rangle$ to $^2P_{1/2}|F = 0\rangle$ transition (linewidth $\gamma/2 \approx 19.6$ MHz) caused photons to scatter off each ion if the qubit was projected to the $|\uparrow\rangle_z$ state. Conversely, ions projected to the $|\downarrow\rangle_z$ qubit state scattered a negligible number of photons because the laser was detuned from resonance by the $^2S_{1/2}$ hyperfine splitting. By applying global $\pi/2$-pulses, we rotated the x and y bases into the z basis. This allowed us to measure all individual magnetizations and many-body correlators along any single axis.

Both systems collected scattered 369.5 nm photons using a finite conjugate 0.4 numerical aperture objective lens system with total magnification of ×70 for System 1 and ×90 for System 2. Before taking data, high-contrast calibration images of the ion chain illuminated by Doppler cooling light were used to identify a region of interest on the camera sensor for each ion. System 2 can take multiple calibration images between experiments to account for slow drift of the ions' positions. During data collection, System 1 (2) integrated collected fluorescence for 0.65 ms (1.0 ms), after which a pre-calibrated binary threshold was applied to discriminate the qubit state of each ion with approximately 97% accuracy per ion. The dominant detection error sources were: off-resonant mixing of qubit states during the detection period, cross-talk between ion regions of interest due to small inter-ion spacings near the centre of the chain, electronic camera noise and laser power fluctuations. We did not perform any post-processing, including state preparation and measurement correction, on the data presented in this work.

Generating the Ising Hamiltonian. We generated spin–spin interactions by applying spin-dependent dipole forces with a pair of non-copropagating 355 nm Raman beams for which the beatnote wavevector, $\Delta\mathbf{k}$, was aligned along the transverse motional modes of the ion chain. These two beams were controlled with acousto-optic modulators that generated a pair of beatnote frequencies $\nu_0 \pm \mu$ for the Mølmer–Sørensen scheme[30], where μ is the frequency detuning from the COM motional mode. In the Lamb–Dicke regime[51], the laser–ion interaction gives rise to an effective spin–spin Hamiltonian where the coupling between spins i and j is:

$$J_{i,j} = \Omega^2 \nu_{\mathrm{R}} \sum_m \frac{b_{i,m} b_{j,m}}{\mu^2 - \nu_m^2} \approx \frac{J_0}{|i-j|^\alpha} \tag{4}$$

where Ω is the resonant Rabi frequency coupling the two qubit states, $\nu_{\mathrm{R}} = \hbar\Delta\mathbf{k}^2/(2M)$ is the recoil frequency, ν_m is the frequency of the mth motional mode, b_{im} is the eigenvector matrix element of the ith ion's participation in the mth motional mode ($\sum_i |b_{im}|^2 = \sum_m |b_{im}|^2 = 1$) and M is the mass of a single ion.

Unlike System 1, where $\Delta\mathbf{k}$ was aligned along one set of transverse motional modes, System 2 coupled to both sets of transverse motional modes as the Raman beams projected onto the two radial principal axes of the trap. Although coupling to these additional modes created the same Hamiltonian (equation (1)) as System 1, the coupling strengths between ions differed. To account for this, equation (4) can be generalized to:

$$J_{i,j} = J^x_{i,j} + J^y_{i,j} \tag{5}$$

$$J^\beta_{i,j} = \Omega_\beta^2 \nu^\beta_{\mathrm{R}} \sum_m \frac{b^\beta_{i,m} b^\beta_{j,m}}{\mu^2 - (\nu^\beta_m)^2}, \ \beta = x, y \tag{6}$$

where ν^β_{R} is the recoil frequency given by the β projection of $\Delta\mathbf{k}$ (Δk^x and Δk^y). Both experiments work in the Mølmer–Sørensen regime where the beatnote frequencies are detuned by μ far from all the motional sidebands, $|\mu - \nu_m| \gg \eta\Omega$, where η is the Lamb–Dicke parameter, to suppress phonon production via virtually coupling spins to motion.

The approximate power law exponent α in equation (4) can theoretically be tuned within the range $0 < \alpha < 3$. However, in practice, we were restricted to $0.5 < \alpha < 1.8$ to avoid motional decoherence and to maintain sufficiently large interaction strengths. Therefore, in this work, we were in the regime where all excitations within the two-domain-wall model were bounded, where $\alpha < 2$ (see the next section for details). In the reported experiments, the power-law exponent was $\alpha = 1.1$ with $J_0/2\pi$ ranging from 0.45 kHz to 0.66 kHz for System 1. System 2 operated in the regime with α between 0.8 and 1 with $J_0/2\pi$ ranging from 0.23 kHz to 0.42 kHz.

We applied a global offset to the two Raman lasers by $2B_z$, creating a rotating frame shift between the qubit and the Raman beatnote to generate an effective transverse magnetic field B_z. We limited the effective transverse B field to $B \ll \eta\Omega_{\mathrm{COM}} \ll \delta_{\mathrm{COM}}$, where $\eta\Omega_{\mathrm{COM}}$ is the COM sideband Rabi frequency and δ_{COM} is the beatnote's detuning from the transverse COM mode.

These trapped-ion quantum simulators natively realized an antiferromagnetic Ising model. All measured observables $O(t)$ of the evolution were real and symmetric under time reversal. This implies that the measured observables of Hamiltonians H and $-H$ are the same. Therefore, the expectation values we obtained from $J_{ij} > 0$ and $B > 0$ are identical to $J_{ij} < 0$ and $B < 0$. For this reason, we could simulate the dynamics of a ferromagnetic system[52].

Two-domain-wall model. Previous experimental and theoretical studies[7,11] found that the low-energy excitations of confinement Hamiltonians, such as equation (1), largely consist of states containing zero or two domain walls. By restricting the Hilbert space to include only these states, we could build a relatively simple phenomenological model that mimicked the low-energy behaviour of the system. Liu et al. described such a 'two-kink model' for a ferromagnetic long-range transverse field Ising chain with closed boundary conditions and $B < J_0$ in ref. [11], which we will summarize here.

The Hilbert space of this model contained states with two down-aligned domains surrounding an up-aligned domain of length l. These domains are separated by two domain walls: one between spin positions $j-1$ and j and another between positions $j+l-1$ and $j+l$. Such a state $|j, l\rangle$ has the form

$$|j, l\rangle = \left|\downarrow_1 \ldots \downarrow \downarrow_{j-1} \uparrow_j \uparrow \ldots \uparrow \uparrow_{j+l-1} \downarrow_{j+l} \downarrow \ldots \downarrow\right\rangle. \tag{7}$$

The Hamiltonian for this set of basis states is given by equation (2) in ref. [11]. For a translational invariant system, it is useful to transform to a set of quasimomentum basis states $|k, l\rangle = (1/L)\sum_{j=1}^{L} \exp(-ikj - ikl/2)|j, l\rangle$. We write the Hamiltonian as

$$\begin{aligned} H = \sum_{k,l} \quad & V(l)|k,l\rangle\langle k,l| - 2B\cos\left(\tfrac{k}{2}\right)|k,l\rangle\langle k,l+1| \\ & -2B\cos\left(\tfrac{k}{2}\right)|k,l\rangle\langle k,l-1|. \end{aligned} \tag{8}$$

Both terms involving the transverse field B describe the effective kinetic energy of the domain walls with quasimomentum k. The potential $V(l)$ depends on the interaction strengths $J_{i,j}$ in the system

$$V(l) = -\sum_{i<j}^{L} J_{i,j} s_i(\mathcal{S}) s_j(\mathcal{S}) \tag{9}$$

where $s_i(\mathcal{S}) = \pm 1$ is the value of the spin at site i corresponding to the configuration $\mathcal{S}$ with domain of length l. This Hamiltonian can be diagonalized to reveal the presence of energy bands in the low-energy spectrum (inset of Fig. 3e). These bands represent domain-wall states bounded by the potential $V(l)$. For $\alpha < 2$ this potential is unbounded and all domain-wall pairs would be confined into quasiparticles.

The linear trapped-ion spin system is finite with open boundary conditions. Boundary effects[53] were minimized in this experiment because the centre-to-centre spin interaction strength is much stronger than the centre-to-edge interaction

strength. To minimize deviations from this model due to finite-size effects, we considered only those states with short, up-aligned domains ($l \ll L$) centred in the spin chain. With this constraint, we found good agreement between exact diagonalization ($L \leq 21$), the two-domain-wall model and experimental results. The two-domain-wall model numerical predictions for this experiment were implemented by taking the experimental $J_{i,j}$ matrix to calculate the energy gaps for each experiment. We first extracted a vector of interaction parameters from the experimental interaction matrix, $J_{k,j}$, by fixing site k as the centre ion for each ion chain length. Then, we virtually placed the ions on a ring and imposed a periodic boundary condition by requiring the Ising interaction to be translationally invariant, that is $J_{l,m}=J_{k,k+m-l}$. Using this method, we obtained the spectrum of energy bands and energy gaps for the trapped-ion system by diagonalizing equation (8) (Fig. 3e).

The two-domain-wall model focused on the potential due to the separation between domain walls, which was largely independent of the centre position of the bound domain-wall pair. We expected some dispersion in the domain-wall pair position due to hopping throughout the spin chain. However, the strength of this hopping was much smaller than the strength of the confining potential. For example, the hopping strength for the initial state with one domain size was on the order of $B^2/\Delta E_{1,2}=0.11J_0$, which corresponded to ~65 Hz in the lab. We expected that this effect would be observed at a timescale (>15 ms) beyond the coherence time of these experiments. Therefore, the domain-wall pairs were expected to be effectively pinned at their original positions over the experimental time, and we did not observe any effects of moving domain-wall pairs in the data. Instead, we observed local coherent oscillations between different bands of bound states.

Energy levels of bound states. The initial state $|n\rangle$ can be written as a superposition of post-quench eigenstates $|s\rangle$

$$|n\rangle = \sum\nolimits_s c_{ns}|s\rangle \tag{10}$$

where c_{ns} is the overlap of $|s\rangle$ with the initial state $|n\rangle$. Thus, any observable M as a function of time is

$$\langle M(t)\rangle = \sum\nolimits_{ss'} c_{ns}c^*_{ns'}\mathrm{e}^{-i(E_s-E')}\langle s'|M|s\rangle \tag{11}$$

where E_s is the energy of state $|s\rangle$. Therefore, $\langle M(t)\rangle$ exhibited oscillation frequencies corresponding to multiple bound-state energy differences, $\Delta E_{s,s'} = E_s - E_{s'}$ with different amplitudes, depending on the initial state. In the experiment, we prepared initial states that overlapped closely with low-energy eigenstates of the confinement Hamiltonian in equation (1) and chose to observe spins on the outer boundaries of the domain walls. This allowed us to maximize the matrix elements ($\langle s'|M|s\rangle$), which couple the lower-energy bound state i to the adjacent higher-energy bound state $i+1$. Therefore, the oscillation frequencies that we observed in Fig. 3 represent $\Delta E_{i,i+1}$. Owing to the limited coherence time of the system, we could not resolve the Fourier spectrum of the dynamics, especially for $\Delta E_{2,3}$, to extract the bound-state energy differences. Instead, we fitted these frequencies to an exponentially decaying sine function. The error bars were the standard errors of these fits (Fig. 3d–f). This fitting choice worked well because we maximized the signal for $\Delta E_{i,i+1}$. $\Delta E_{i,i+1}$ also decreased as the energy level i increased (inset of Fig. 3e). Using this knowledge, we could measure $\Delta E_{i,i+1}$ starting from the lowest-energy initial state (all x polarized) to the higher-energy initial state (two domain walls with a domain size of two). Then, we took a suitable single frequency as a guess value for fitting the quench dynamics. The guess value was chosen such that it was the next lowest frequency from the oscillation frequency measured in the lower-energy initial state (Supplementary Section 2.3). In the end, this method yielded results that matched closely with the two-domain-wall model and numerical predictions calculated by solving the Schrödinger equation. For a complete picture, the Fourier-transformed experimental data are also shown in the Supplementary Information.

Domain-wall convergence at high transverse B field. In this domain-wall investigation, we used the following Bloch sphere mapping: $z \leftrightarrow x$. The orientation of the ith spin in the Bloch sphere is defined as $|\psi_i(t)\rangle = \cos\theta(t)/2|0\rangle + \mathrm{e}^{i\phi}\sin\theta(t)/2|1\rangle$. Let $|\psi\rangle = |\psi_i(t)\rangle \otimes |\psi_{i+1}(t)\rangle$ since we were interested in a two-body correlator for $\langle\mathcal{N}\rangle$. At high transverse B field, global Larmor precession about the transverse direction dominated over the Ising interaction term in equation (1). The expectation value of the two-body correlator along z was $\langle\sigma^z_i(t)\sigma^z_{i+1}(t)\rangle = 1 - \sin^2(\theta(t))$. Inserting $\langle\sigma^z_i(t)\sigma^z_{i+1}(t)\rangle$ into equation (3) gives

$$\langle\mathcal{N}\rangle = \frac{1}{t_2 - t_1}\int_{t_1}^{t_2}\sum\nolimits_i^{L-1}\frac{\sin^2(\theta(t))}{2}\mathrm{d}t. \tag{12}$$

Therefore, $\langle\mathcal{N}\rangle = 0.25(L-1)$ when $B \gg J_0$. Values of t_1 and t_2 were chosen to include the plateaus of $\langle\mathcal{N}\rangle$ while excluding dephasing of the spins. We fixed the scaled integration time $J_0(t_2-t_1)$, as J_0 differed with system size (Extended Data Fig. 1).

We note that the last experiment, data from which are presented in Fig. 4, bears resemblance to a previous experiment published by Zhang et al.[28]. Both experiments involved measuring an observable related to a two-spin magnetization correlator and its dependence on the transverse field strength of a quenched Ising Hamiltonian. The two-spin correlator defined in ref. [28] was expected to be qualitatively similar to the average number of domain walls (equation (3)).

Several notable aspects distinguish the experiment shown in Fig. 4 from those in ref. [28]. Each experiment was performed with different scopes and goals. The goal of ref. [28], performed in System 1, was to identify the precise critical point of a dynamical phase transition, whereas this experiment, performed in System 2, was designed to contrast the behaviour of a spin system deep in the confinement regime ($B \ll J_0$) with behaviour deep in the deconfinement regime ($B \ll J_0$) using an observable derived from the confined-quasiparticle picture. The confinement picture provides valuable context for understanding the dynamics observed in each regime.

Error sources. Experimental noise decreases the fidelity of any quantum simulation. All the possible sources of error described here were consistently present in the experiment. However, the effects of certain noise sources are different depending on the observable.

One substantial error is bit-flip error, which we attributed to two main sources. One source was spin-motion entanglement due to off-resonant excitation of the ion chain's motional modes[54] in the Mølmer–Sørensen regime, where both quantum simulators operate. Unwanted bit-flip errors occur when spin-entangled motional degrees of freedom are traced out at the end of an experiment. The probability of this error occurring on the ith ion is proportional to $\sum_{m=1}^{N}(\eta_{im}\Omega/\delta_m)^2$, where $\eta_{im} = b_{im}\sqrt{\nu_R/\nu_m}$ and $\delta_m = \mu - \nu_m$ is the beatnote detuning from the mth motional mode[55]. To minimize this error, we chose δ_{COM} such that $(\eta_{\mathrm{COM}}\Omega/\delta_{\mathrm{COM}})^2 \lesssim 1/9$. Another source of bit-flip error was imperfect state detection. These two sources of bit-flip error were independent, and therefore add in quadrature. This error affected the observable $\langle\mathcal{N}\rangle$ because it induced errors in counting the number of domain walls. We found that, by including the bit-flip error in the $L=11$ spins numerical calculation for $\langle\mathcal{N}\rangle$, the experimental data agreed well with the error-included numerical calculation at $B/J_0=0$, as shown in Extended Data Fig. 2. At present, we are limited to computing this error for $L<15$ spins. Regarding individual spin magnetization and connected-correlation observables, this bit-flip error will decrease the contrast of the spin magnetization. The qualitative features, as well as oscillation frequencies, will remain unchanged.

Besides that, slow experimental drifts, involving laser intensity noise at the ions and drifts of the trap frequency (which determines transverse motional modes for generating the Ising interaction), influenced the experiment over the course of a few hours during data taking. These fluctuations would cause the system to average over different effective Hamiltonians that can be approximated as ±10% fluctuations in J_0 for numerical predictions. For longer spin chains, this effect was more prominent as $1/J_0$ is on the order of the experiment sequence duration (Supplementary Information).

Furthermore, this system had a residual effective linear magnetic field gradient across the ion chains due to the fourth-order a.c. Stark shift gradient from imperfect overlap of the two Raman laser beams at the ions. This effective magnetic gradient noise was more prominent for small B fields and was typically $<15\,\mathrm{Hz\,\mu m^{-1}}$ across the ion chain. As a result, there was an effective depolarization of the initial states, which is depicted clearly in the data in Fig. 4. However, we found that errors caused by this effective magnetic field gradient were much smaller than those caused by bit-flip errors.

Another source of noise is off-resonant Raman scattering during the quantum quench. This error rate was estimated to be 7×10^{-5} Hz per ion, given typical experimental parameters. Small errors due to radiofrequency heating of the transverse COM motional mode were present in System 1. Although System 2 was in a cryogenic set-up that is less susceptible to radiofrequency heating, it had mechanical vibrations at 41 Hz and 39 Hz due to residual mechanical coupling to the cryostat[33]. This mechanical vibration noise is equivalent to phase noise on the Raman beams, which led to qubit dephasing. Therefore, we integrated the number of domain walls before the dephasing occurred (Fig. 4).

Data availability

The data presented in the figures of this Article are available from the corresponding authors upon reasonable request.

Code availability

All custom code used to support claims and analyse data presented in this Article is available from the corresponding authors upon reasonable request.

References

50. Mølmer, K. & Sørensen, A. Multiparticle entanglement of hot trapped ions. *Phys. Rev. Lett.* **82**, 1835–1838 (1999).
51. Wineland, D. J. et al. Experimental issues in coherent quantum-state manipulation of trapped atomic ions. *J. Res. Natl Inst. Stand. Technol.* **103**, 259–328 (1998).
52. Schachenmayer, J., Lanyon, B. P., Roos, C. F. & Daley, A. J. Entanglement growth in quench dynamics with variable range interactions. *Phys. Rev. X* **3**, 031015 (2013).

53. Neyenhuis, B. et al. Observation of prethermalization in long-range interacting spin chains. *Sci. Adv.* **3**, e1700672 (2017).
54. Joseph Wang, C.-C. & Freericks, J. K. Intrinsic phonon effects on analog quantum simulators with ultracold trapped ions. *Phys. Rev. A* **86**, 032329 (2012).
55. Wu, Y. *Quantum Computation in Large Ion Crystals*. PhD thesis, Univ. Michigan (2019).

Acknowledgements

We thank D. A. Abanin, P. Bienias, P. Calabrese, M. Dalmonte, Z. Davoudi, A. Deshpande, A. Gambassi, M. Heyl, A. Lerose, J. Preskill, A. Silva, P. Titum and R. Verdel for enlightening discussions. This work was supported by the NSF PFCQC STAQ programme, the AFOSR MURIs on Quantum Measurement/Verification, the ARO MURI on Modular Quantum Systems, the AFOSR and ARO QIS and AMO Programmes, the DARPA DRINQS programme, DOE BES award number DE-SC0019449, DOE HEP award number DE-SC0019380 and the NSF QIS programme. F.L. also acknowledges support from the Ann G. Wylie Dissertation Fellowship of the University of Maryland. Specific product citations are for the purpose of clarification only, and are not an endorsement by the authors or NIST.

Author contributions

F.L. and G.P. suggested the research topic. W.L.T., P.B., G.P., K.S.C., A.D., L.F., H.B.K., A.K., W.M. and C.M. contributed to the experimental design, construction, data collection and analysis. F.L., R.L., S.W., K.S.C., W.L.T., P.B. and G.P. carried out numerical simulations. F.L., R.L., S.W. and A.V.G. provided theoretical support. All authors contributed to the discussion of the results and the manuscript.

Competing interests

C.M. is Co-Founder and Chief Scientist at IonQ, Inc.

Additional information

Extended data is available for this paper at https://doi.org/10.1038/s41567-021-01194-3.

Supplementary information The online version contains supplementary material available at https://doi.org/10.1038/s41567-021-01194-3.

Correspondence and requests for materials should be addressed to W.L.T. or P.B.

Peer review information *Nature Physics* thanks Roee Ozeri and other, anonymous, reviewer(s) for their contribution to the peer review of this work.

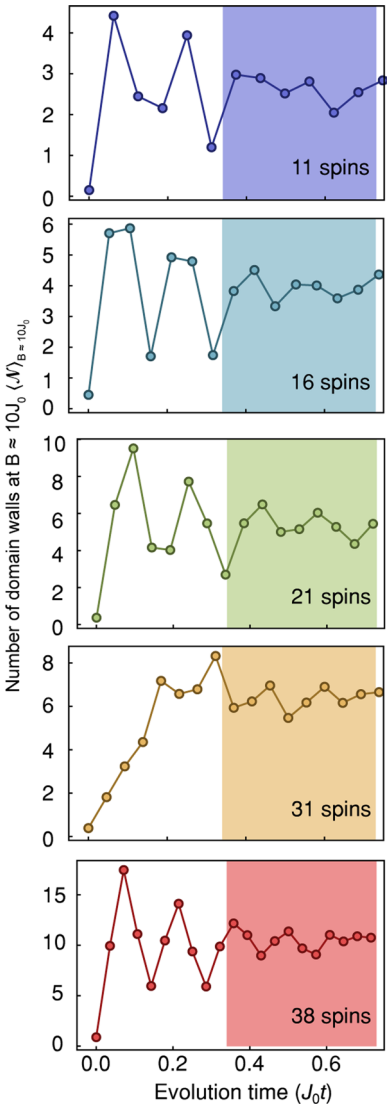

Extended Data Fig. 1 | Evolution of domain wall population. Experimental data of evolution of the number of domain walls $\langle \mathcal{N} \rangle$ during a quench of Hamiltonian (1) with $B/J_0 \approx 10$ for multiple system sizes. The shaded area indicates when $\langle \mathcal{N} \rangle$ converges to a steady state and before qubit dephasing occurs.

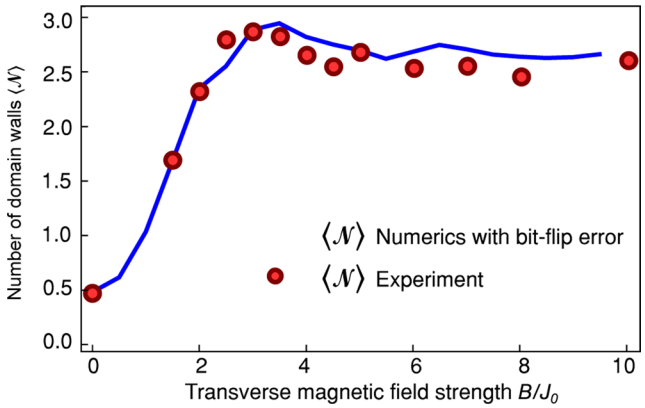

Extended Data Fig. 2 | Bit-flip error numerical study in $L=11$ chain for dynamical regimes investigation. Red dots show the $L=11$ data displayed in Fig. 4a. The blue line illustrates the numerical value of $\langle\mathcal{N}\rangle$ with increasing B-field, taking bit-flip error into account. We found that a bit-flip error per ion of 2.47% in the numerical calculation matches the experimental data well. The most notable effect of bit-flip errors is an increase in the number of domain walls at $B/J_0=0$ (see Fig. 4a for comparison with the zero bit-flip error numerical predictions).